



# Experimental determination and thermodynamic assessment of the Dy-Fe-B system



Wei Yang <sup>a,b</sup>, Yiwei Wang <sup>c</sup>, Shuhong Liu <sup>a</sup>, Peisheng Wang <sup>a,b,\*</sup> Wei Zhai <sup>d</sup>

<sup>a</sup> Powder Metallurgy Research Institute, Central South University, 410083, Changsha, PR China

<sup>b</sup> Hunan Key Laboratory of Advanced Fibers and Composites, Central South University, 410083, Changsha, PR China

<sup>c</sup> Hunan Boxiang New Materials, Ltd., 410000, Changsha, PR China

<sup>d</sup> School of Physical Science and Technology, Northwestern Polytechnical University, 710072, Xi'an, PR China

## ARTICLE INFO

Handling Editor: Prof. Z.K. Liu

### Keywords:

Isothermal sections

Compounds

## ABSTRACT

The phase equilibria of the Fe-Dy-B system on the Fe-Dy side are crucial for the development of Nd-Dy-Fe-B permanent magnets. Alloys located on the Fe-Dy side were prepared and annealed at 1073 K and 1173 K for 60 days. The annealed samples were analyzed by electron probe microanalysis (EPMA) and X-ray diffraction (XRD). In this work, three ternary compounds  $\tau_1$ ,  $\tau_3$ , and  $\tau_4$  were identified on the Fe-Dy side at 1073 K and 1173 K. The previously reported  $\tau_2$  phase was not observed in the present work. Nine three-phase regions were determined in the present study and the isothermal sections of the Dy-Fe-B system on the Dy-Fe side at 1073 K and 1173 K were constructed. Based on the experimental data, thermodynamic modeling of the system was performed using the CALculation of PHase Diagrams (CALPHAD) method. The calculated results show good agreement with the experimental data.

## 1. Introduction

Rare-earth (RE) permanent magnet based on  $\text{Nd}_2\text{Fe}_{14}\text{B}$  exhibit strong magnetic flux density and uniaxial magnetic anisotropy [1,2]. As a result,  $\text{Nd}_2\text{Fe}_{14}\text{B}$  rare-earth permanent magnets have been widely used in electric vehicles, wind power generation systems, and consumer electronics. However, their low Curie temperature and coercivity limit their performance. In contrast,  $\text{Dy}_2\text{Fe}_{14}\text{B}$  has a higher coercivity [3,4], making Dy a valuable additive to partially replace Nd in commercial rare-earth permanent magnets. Nonetheless, the  $\text{Dy}_2\text{Fe}_{14}\text{B}$  has a lower remanence deterioration due to its ferrimagnetic nature. The CALPHAD-type (CALculation of PHase Diagrams) simulation is a powerful tool for materials design. For the permanent magnets, a well-established CALPHAD database is essential for understanding the microstructures, the formation of the primary and second compounds and the magnetic properties of the rare-earth permanent magnets. The phase equilibria of the Dy-Fe-B system have been experimentally studied by Chernyak et al. [5]. The samples were prepared through arc melting from the compacted Fe-B powders and solid Dy. The samples were then annealed at 1070 K for at least 700 h. The annealed samples were analyzed by X-ray diffraction. Six ternary compounds  $\text{Dy}_2\text{Fe}_{14}\text{B}(\tau_1)$ ,  $\text{DyFe}_2\text{B}_2(\tau_2)$ ,  $\text{DyFe}_4\text{B}_4(\tau_3)$ ,  $\text{Dy}_5\text{Fe}_2\text{B}_4(\tau_4)$ ,  $\text{Dy}_3\text{Fe}_7(\tau_5)$ , and  $\text{DyFe}_4\text{B}_4(\tau_6)$

were identified and the isothermal section at 1073 K was constructed. However, Chernyak et al. [5] provide limited details regarding their findings.

Grieb et al. [6] investigated the iron-rich regions of the Dy-Fe-B system. Four vertical sections were determined using Differential Thermal Analysis (DTA) and microstructure analysis. Their study revealed that a maximum of 5 at.% B dissolves in the binary compound  $\text{Dy}_2\text{Fe}_{17}$  above 1473 K and suggested that B behaves as a substitutional element for Fe in a solid solution. However, no thermodynamic data were reported for the ternary compounds or liquid phase were provided.

The thermodynamic description for the Dy-Fe-B system was done by several groups [7–9]. However, none of these studies provide a comprehensive description of the Dy-Fe-B system and only the ternary compounds  $\text{Dy}_2\text{Fe}_{14}\text{B}$  and  $\text{DyFe}_4\text{B}_4$  have been considered.

This work aims to investigate the phase equilibria of the Dy-Fe-B system and construct the isothermal sections of the system on the Fe-Dy rich side at 1073 K and 1173 K. A CALPHAD-based thermodynamic assessment of the Dy-Fe-B system is also performed to provide a self-consistent thermodynamic description.

\* Corresponding author.

E-mail address: [peisheng.wang@outlook.com](mailto:peisheng.wang@outlook.com) (P. Wang).

**Table 1**

The crystallographic information for the binary phases of the Dy-Fe-B system.

Phase name	Crystallographic information				Reference
	Strukturbericht	Prototype	Pearson symbol	Space group	
( $\alpha$ -Dy)	A3	Mg	hp2	P6 <sub>3</sub> /mmc	[25]
( $\beta$ -Dy)	A2	W	cI2	I $m\bar{3}m$	[25]
( $\alpha$ -Fe)	A2	W	cI2	I $m\bar{3}m$	[26]
( $\gamma$ -Fe)	A1	Cu	cF4	Fm $\bar{3}m$	[26]
( $\delta$ -Fe)	A2	W	cI2	I $m\bar{3}m$	[26]
( $\beta$ -B)	B	B	rR423	R $\bar{3}m$	[27]
Dy <sub>2</sub> Fe <sub>17</sub>	Dy <sub>2</sub> Fe <sub>17</sub>	Th <sub>2</sub> Ni <sub>17</sub>	hR57	R $\bar{3}m$	[28]
Dy <sub>6</sub> Fe <sub>23</sub>	Dy <sub>6</sub> Fe <sub>23</sub>	Th <sub>2</sub> Mn <sub>23</sub>	cF116	Fm $\bar{3}m$	[28]
DyFe <sub>3</sub>	DyFe <sub>3</sub>	Be <sub>3</sub> Nb	hR36	R $\bar{3}m$	[28]
DyFe <sub>2</sub>	DyFe <sub>2</sub>	MgCu <sub>2</sub>	cF24	Fd $\bar{3}m$	[28]
DyB <sub>66</sub>	DyB <sub>66</sub>	YB <sub>66</sub>	cF1936	Fm $\bar{3}c$	[29]
DyB <sub>12</sub>	DyB <sub>12</sub>	UB <sub>12</sub>	cF52	Fm $\bar{3}m$	[29]
DyB <sub>6</sub>	DyB <sub>6</sub>	CaB <sub>6</sub>	cP7	Pm $\bar{3}m$	[29]
DyB <sub>4</sub>	DyB <sub>4</sub>	UB <sub>4</sub>	tP20	P4/mbm	[29]
DyB <sub>2</sub>	DyB <sub>2</sub>	AlB <sub>2</sub>	hp3	P6 <sub>3</sub> /mmm	[25]
FeB	FeB	FeB	oP8	Pnma	[30]
Fe <sub>2</sub> B	Fe <sub>2</sub> B	CuAl <sub>2</sub>	tI12	I <sub>4</sub> /mcm	[30]
$\tau_1$	Dy <sub>2</sub> Fe <sub>14</sub> B	Nd <sub>2</sub> Fe <sub>14</sub> B	tP68	P42/mnm	[31]
$\tau_2$	DyFe <sub>2</sub> B <sub>2</sub>	CeAl <sub>2</sub> Ga <sub>2</sub>	tI10	I4/mmm	[32]
$\tau_3$	DyFe <sub>4</sub> B <sub>4</sub>	NdFe <sub>4</sub> B <sub>4</sub>	tP*	P4/ncc	[33]
$\tau_4$	Dy <sub>5</sub> Fe <sub>2</sub> B <sub>4</sub>	Nd <sub>5</sub> Fe <sub>2</sub> B <sub>6</sub>	hR13	R $\bar{3}m$	[34]
$\tau_5$	Dy <sub>3</sub> FeB <sub>7</sub>	Er <sub>3</sub> CrB <sub>7</sub>	oS44	Cmcm	[35]
$\tau_6$	DyFeB <sub>4</sub>	CrYB <sub>4</sub>	aP24	Pbam	[36]

**Table 2**

Summary of the SEM-EPMA experimental results of the alloys (in at.%) annealed at 1173 K (components with small phase fractions that are difficult to measure are marked \* in the remark).

Nº	Nominal composition			Phases	Phase Composition			Remark
	Dy	Fe	B		Dy	Fe	B	
A1	1.00	88.90	10.11	Fe <sub>2</sub> B ( $\alpha$ Fe) $\tau_3$ $\tau_1$ $\tau_3$	0.05 0.14 9.03 0.14 11.96	62.51 99.85 49.65 99.85 82.87	37.44 0.02 41.32 0.02 5.17	*
A2	4.95	89.68	5.37	( $\alpha$ Fe) $\tau_1$ $\tau_3$	0.15 10.34 12.51 22.04 26.35 12.98 21.85 26.11 12.94 22.45 26.90 13.55 27.11 35.55 13.86 26.94 35.29 13.38 35.23 35.14 13.97 14.24 35.14 13.97 18.86	99.85 89.66 81.75 77.63 73.44 81.58 78.15 73.52 82.23 77.18 73.02 44.06 72.75 63.88 43.06 73.06 64.71 41.07 64.75 64.01 43.33 44.18 43.08 0.00 0.57 5.43 0.14 0.00 0.37 4.83 0.38 0.08 42.39 0.14 0.57 43.08 0.00 0.00 45.55 41.58	0.00 0.00 5.74 0.33 0.20 5.43 0.00 0.37 4.83 0.38 0.08 42.39 0.14 0.57 43.08 0.00 0.00 45.55 41.58	*
A3	7.49	90.56	1.95	( $\alpha$ Fe) Dy <sub>2</sub> Fe <sub>17</sub> $\tau_1$ Dy <sub>6</sub> Fe <sub>23</sub> DyFe <sub>3</sub> $\tau_1$ Dy <sub>6</sub> Fe <sub>23</sub> DyFe <sub>3</sub> $\tau_1$ Dy <sub>6</sub> Fe <sub>23</sub> DyFe <sub>3</sub> $\tau_1$ Dy <sub>6</sub> Fe <sub>23</sub> DyFe <sub>3</sub> $\tau_3$ DyFe <sub>3</sub> DyFe <sub>2</sub> $\tau_3$ DyFe <sub>3</sub> DyFe <sub>2</sub> $\tau_3$ DyFe <sub>3</sub> DyFe <sub>2</sub> $\tau_4$ DyFe <sub>2</sub> $\tau_3$ $\tau_4$ Liquid	0.15 10.34 12.51 22.04 26.35 12.98 21.85 26.11 12.94 22.45 26.90 13.55 27.11 35.55 13.86 26.94 35.29 13.38 35.23 35.14 13.97 14.24 35.14 13.97 18.86	99.85 89.66 81.75 77.63 73.44 81.58 78.15 73.52 82.23 77.18 73.02 44.06 72.75 63.88 43.06 73.06 64.71 41.07 64.75 64.01 43.33 44.18 43.08 0.00 0.00 45.55 41.58	0.00 0.00 5.74 0.33 0.20 5.43 0.00 0.37 4.83 0.38 0.08 42.39 0.14 0.57 43.08 0.00 0.00 45.55 41.58	*
A4	16.33	81.70	1.97					
A5	21.01	77.04	1.95					
A6	24.95	73.06	1.99					
A7	28.23	66.74	5.04					
A8	32.03	62.97	5.00					
A9	32.98	61.98	5.04					
A10	33.87	60.96	5.17					
A11	38.19	58.81	3.00					

## 2. Methodology

### 2.1. Experimental procedures

The crystallographic data of the binary and ternary systems are listed in Table 1.

Twenty-two ternary alloys with varying compositions were prepared by arc-melting 99.99 wt% Dy, 99.99 wt% Fe, and 99.99 wt% B (Zhong Nuo Advanced Material Technology Co., Ltd., Beijing, China) in a vacuum arc-melting furnace (WK-I, Physcience Opto-electronics Co., Ltd. Beijing, China) with a water-cooled copper crucible under a 99.999 % pure Ar atmosphere. Every sample was melted at least five times to ensure homogeneity and the mass loss was controlled below 1 wt%. The as-cast samples were sealed in evacuated quartz capsules with a vacuum sealing machine (MRVS-1002, Wuhan Bailibo Technology Co., Ltd., China) after surface polishing, and annealed at 1073 K and 1173 K for 60 days. Thereafter, the samples were quenched in water.

The composition of both as-cast and annealed specimens was analyzed by electron probe microanalysis (EPMA, JXA-8530, JEOL, Japan) at 15 kV using pure Dy (99.99 wt%), Fe (99.99 wt%), and B (99.99 wt%) as standard materials. The phase constitutions were identified by X-ray diffraction (XRD) using a diffractometer with Cu K $\alpha$  radiation. The diffraction pattern was obtained in a scanning step of 0.02° and a scanning speed of 0.75 s/step, with a scanning angle exceeding 20° range 20–90°. The crystal structures of the formed phases were refined using the Rietveld refinement technique with Fullprof software.

### 2.2. Thermodynamic models

#### 2.2.1. Pure element

The descriptions of the Gibbs energies of the pure elements Dy, Fe,

**Table 3**

Summary of the SEM-EPMA experimental results of the alloys (in at.%) annealed at 1073 K (components with small phase fractions that are difficult to measure are marked \* in the remark).

Nº	Nominal composition			Phases	Phase Composition			Remark
	Dy	Fe	B		Dy	Fe	B	
B1	2.48	20.15	77.37	Fe <sub>2</sub> B (αFe)	0.07 0.31	63.55 99.69	36.38 0.00	*
B2	9.37	20.11	70.52	τ <sub>3</sub> (αFe)	0.35	99.58	0.07	*
B3	19.36	20.11	60.53	τ <sub>3</sub> τ <sub>1</sub> DyFe <sub>3</sub>	12.99 26.31	44.68 73.69	42.33 0.00	*
B4	24.95	20.23	54.82	τ <sub>4</sub> DyFe <sub>2</sub>	42.57 34.33	21.33 65.44	36.11 0.23	*
B5	28.96	21.23	49.81	τ <sub>3</sub> DyFe <sub>2</sub>	13.42 34.51	44.14 65.22	42.44 0.27	
B6	32.14	20.94	46.93	τ <sub>4</sub> DyFe <sub>2</sub>	39.81 34.67	24.42 65.12	35.78 0.22	
B7	33.95	20.46	45.60	τ <sub>3</sub> DyFe <sub>2</sub>	13.39 34.66	43.32 65.05	43.29 0.29	
B8	51.43	20.33	28.24	τ <sub>4</sub> (αDy) DyFe <sub>2</sub>	42.75 97.83 34.86	19.95 2.17 64.58	37.31 0.00 0.56	
B9	9.95	2.64	87.41	τ <sub>4</sub> (αFe) Dy <sub>2</sub> Fe <sub>17</sub>	45.68 0.95 10.16	18.13 99.05 89.46	36.20 0.00 0.37	
B10	15.47	2.82	81.71	τ <sub>1</sub> Dy <sub>2</sub> Fe <sub>17</sub> Dy <sub>6</sub> Fe <sub>23</sub>	12.39 10.80 21.60	82.81 89.02 78.40	4.79 0.18 0.00	
B11	14.80	5.80	79.40	τ <sub>1</sub> Dy <sub>6</sub> Fe <sub>23</sub> DyFe <sub>3</sub>	21.49 25.62 12.63	78.51 73.92 83.17	0.00 0.45 4.20	

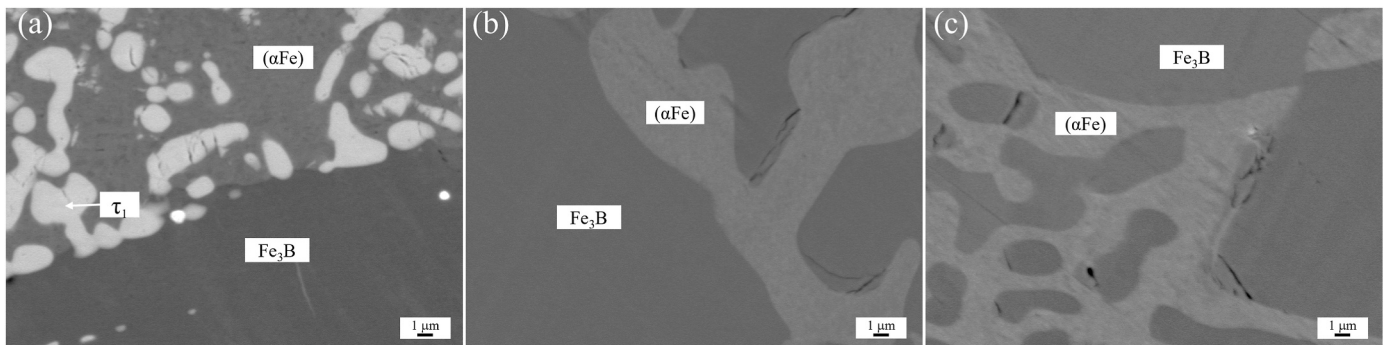


**Fig. 1.** (a) The BSE micrographs of the composition Fe<sub>77</sub>B<sub>20</sub>Dy<sub>3</sub> alloy annealed at 1173 K for 60 days; (b) As-cast alloys FeB<sub>20</sub>; (c) Alloys FeB<sub>20</sub> furnace cooled at 1423 K for 10 h.

and B were taken from the pure element thermodynamic database of the SGTE (Version 5.1) [10].

### 2.2.2. Solution phases

The Gibbs energy for the solution phases G<sub>m</sub><sup>φ</sup> ( $\phi = \text{Liquid, FCC\_A1, BCC\_A2, and HCP\_A3}$ ) were described by the substitutional solution model with Redlich–Kister polynomials [11].

$$G_m^\phi(T) = \sum_i x_i G_i^\phi(T) + RT \sum_i x_i \ln x_i + {}^E G_m^\phi + {}^{\text{mag}} G_m^\phi \quad (1)$$

where x<sub>i</sub> denotes the molar fractions of the pure elements i (i = Dy, Fe, and B); <sup>E</sup>G<sub>m</sub><sup>φ</sup> is the molar excess Gibbs energy and <sup>mag</sup>G<sub>m</sub><sup>φ</sup> ( $\phi = \text{FCC\_A1, BCC\_A2, and HCP\_A3}$ ) is the magnetic contribution to the molar Gibbs

energy. The thermodynamic parameters of binary solution phases (Dy-Fe, Dy-B, and Fe-B) in this work were selected from the data evaluated by Rong et al. [12], Li et al. [13], and Witusiewicz et al. [14].

### 2.2.3. Intermetallic compounds

The Dy-Fe-B system contains 12 binary intermetallic compounds and 6 ternary intermetallic compounds. The binary intermetallic compounds including four Dy-Fe intermetallic compounds (Dy<sub>2</sub>Fe<sub>17</sub>, Dy<sub>6</sub>Fe<sub>23</sub>, DyFe<sub>2</sub>, and DyFe<sub>3</sub>), five Dy-B intermetallic compounds (DyB<sub>2</sub>, DyB<sub>4</sub>, DyB<sub>6</sub>, DyB<sub>12</sub>, and DyB<sub>66</sub>) and three Fe-B intermetallic compounds (FeB, Fe<sub>2</sub>B and Fe<sub>3</sub>B) were optimized by Rong et al. [12], Li et al. [13], and Witusiewicz et al. [14], respectively. These thermodynamic parameters were selected in this work.

Three ternary intermetallic compounds Dy<sub>2</sub>Fe<sub>14</sub>B(τ<sub>1</sub>), DyFe<sub>4</sub>B<sub>4</sub>(τ<sub>3</sub>),

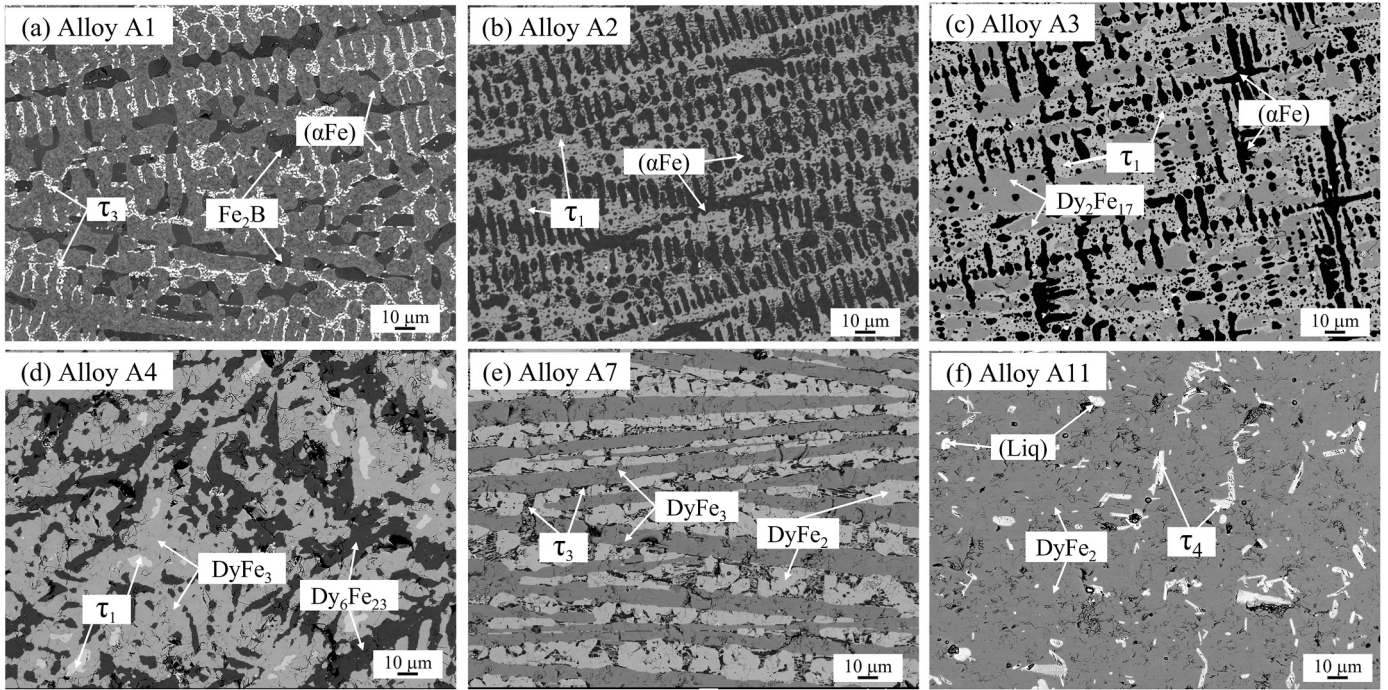


**Fig. 2.** The BSE micrographs of the representative Dy-Fe-B alloys annealed at 1173 K for 60 days: (a) Alloy A1; (b) Alloy A2; (c) Alloy A3; (d) Alloy A4; (e) Alloy A7; (f) Alloy A11.

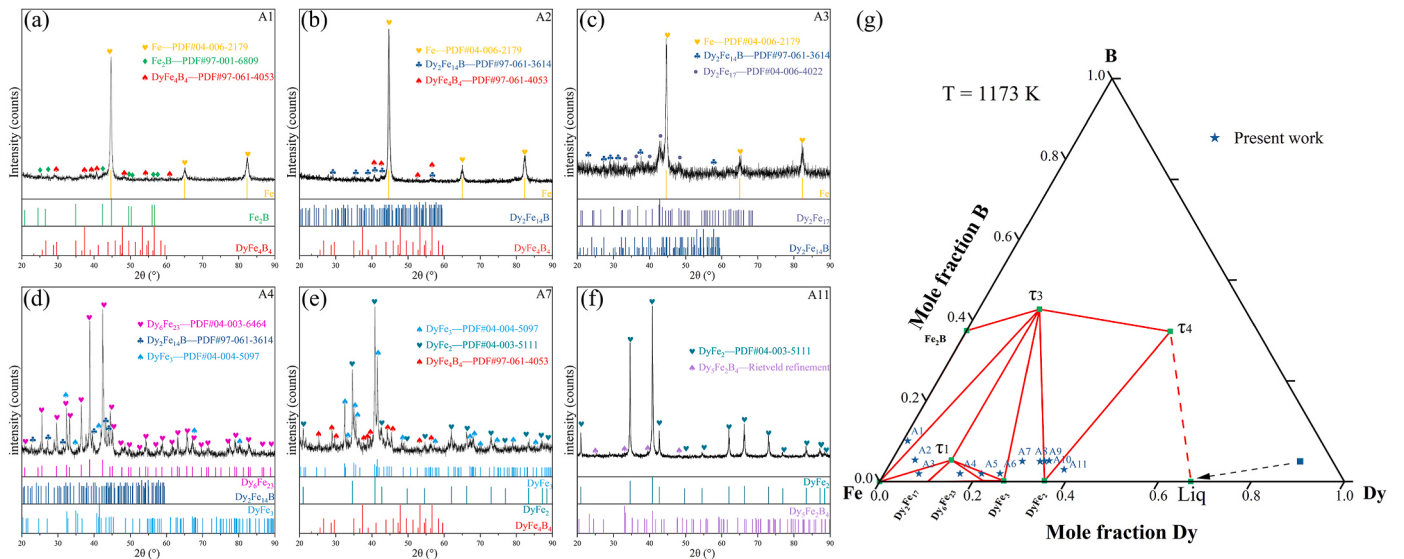


**Fig. 3.** The XRD results of the representative alloys (a–f):A1, A2, A3, A4, A7, and A11; (g) The experimentally determined isothermal sections of the Dy-Fe-B system at 1173 K.

**Table 4**

Details of Rietveld refinement performed on the powder XRD data of  $\tau_4$ - $Dy_5Fe_2B_4$ .

Parameter	Data
Structure refined	$Dy_5Fe_2B_4$ - $Dy_2Fe_{0.8}B_{1.65}$
Space group	$R\bar{3}m$
Pearson symbol	hR13
Unit cell parameter [nm]	$a = 5.4079$ , $c = 22.891$
Reliability factors	$R_p = 9.47\%$ , $R_{wp} = 11.99\%$ , $\chi^2 = 1.19$

and  $Dy_5Fe_2B_4(\tau_4)$  confirmed experimentally in this work and the other two ternary intermetallic compounds  $Dy_3Fe_7(\tau_5)$  and  $DyFe_4(\tau_6)$  reported by Grieb et al. [6] were considered and treated as stoichiometric compounds.

The selection of a thermodynamic model for a stoichiometric compound depends on the available experimental data. The compounds with heat capacity available were described by the formula:

$$G^{r1}(T) = A + BT + CT \ln T + DT^2 + ET^3 + FT^{-1} + GT^7 + HT^{-9} + IT^4 + J \ln T \quad (2)$$

For the stoichiometric compounds without the heat capacity data were evaluated by the formula:

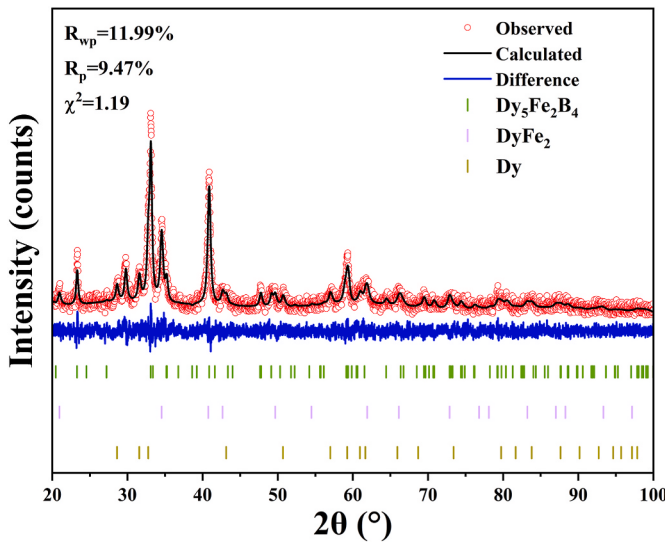


**Fig. 4.** XRD refinement map of Alloy B8.

$$G^\varphi(T) = a^\varphi + b^\varphi T + x_{\text{Dy}}^\varphi G_{\text{Dy}}^{0,\text{hsr}} + x_{\text{Fe}}^\varphi G_{\text{Fe}}^{0,\text{hsr}} + x_{\text{B}}^\varphi G_{\text{B}}^{0,\text{hsr}} \quad (3)$$

where the parameters,  $a^\varphi$  and  $b^\varphi$  were to be optimized.

Several stoichiometric phases in the Dy–Fe–B system exhibit magnetic transitions associated with Neel or Curie temperatures. The Curie temperature (ferromagnetic transition) typically occurs above 298 K. The magnetic contribution to the Gibbs energy was considered by an empirical relationship suggested by Inden [15] and modified by Hillert and Jarl [16].

### 3. Results and discussions

#### 3.1. Experimental results

Representative alloys were prepared to investigate the phase equilibria and phase transitions of the Dy–Fe–B system by EPMA and XRD. The detailed experimental results are summarized in [Tables 2 and 3](#).

##### 3.1.1. Metastable phase $\text{Fe}_3\text{B}$

[Fig. 1](#) shows the SEM results for the alloy  $\text{Fe}_{77}\text{B}_{20}\text{Dy}_3$ . The  $\text{Fe}_3\text{B}$  phase was observed, which is known to be metastable, and forms when the B content ranges between 12 and 25 at.% [17]. In this work, a  $\text{FeB}_{20}$  alloy was prepared through arc-melting and held at 1423 K (a temperature between the stable and metastable phase diagram reaction ranges) for 10 h and slowly cooled to room temperature in a furnace. Despite this, the  $\text{Fe}_3\text{B}$  metastable phase still persisted. To prevent the formation of the metastable  $\text{Fe}_3\text{B}$  phase, the B content must be controlled below 12 at.%.

##### 3.1.2. Phase equilibria at 1173 K

Alloys A1–A11 were prepared to determine the isothermal section of the Dy–Fe–B system on the Fe–Dy side at 1173 K. The phase compositions and microstructures were analyzed using SEM–EPMA and XRD. The experimental results are summarized in [Table 2](#). [Fig. 2\(a–f\)](#) and [3\(a–f\)](#) present the backscattered electron (BSE) images and XRD patterns of alloys A1, A2, A3, A4, A7, and A11, respectively after annealing at 1173 K for 60 days.

Based on SEM–EPMA measurements, three phases were observed as shown in [Fig. 2\(a\)](#). Two of these phases were identified as ( $\alpha\text{Fe}$ ) and  $\text{Fe}_2\text{B}$  while the third phase ( $\tau_3$ ) is too fine to accurately determine its composition by EPMA. Nonetheless, the XRD patterns corresponding to the  $\tau_3$  phase were observed as shown in [Fig. 3\(a\)](#). [Fig. 2\(b\)](#) shows that alloy A2 consists of ( $\alpha\text{Fe}$ ) and  $\tau_1$  phases. Due to the low B content of the alloy (less than 5 at%), the phase fraction of  $\tau_3$  is small, thus the peaks in [Fig. 3\(b\)](#) are not weak. However, the  $\tau_3$  phase can be observed in alloy B2 which has a higher B content (20 at%). [Fig. 2\(c\)](#) illustrates that alloy A3 consists of ( $\alpha\text{Fe}$ ),  $\text{Dy}_2\text{Fe}_{17}$  and  $\tau_1$  phases, which aligns with their XRD patterns in [Fig. 3\(c\)](#). [Figs. 2\(d\) and 3\(d\)](#) indicate that alloy A4 consists of

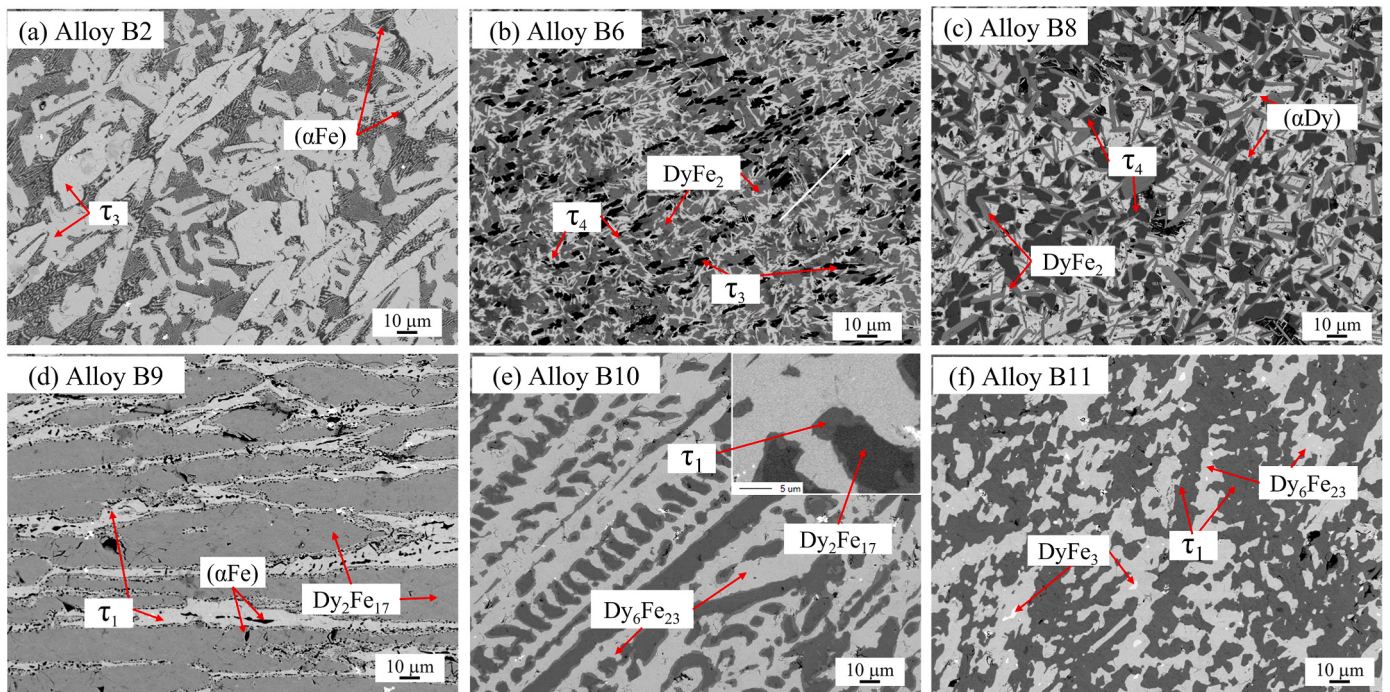


**Fig. 5.** The BSE micrographs of the representative Dy–Fe–B alloys annealed at 1073 K for 60 days: (a) Alloy B2; (b) Alloy B6; (c) Alloy B8; (d) Alloy B9; (e) alloy B10; (f) alloy B11.

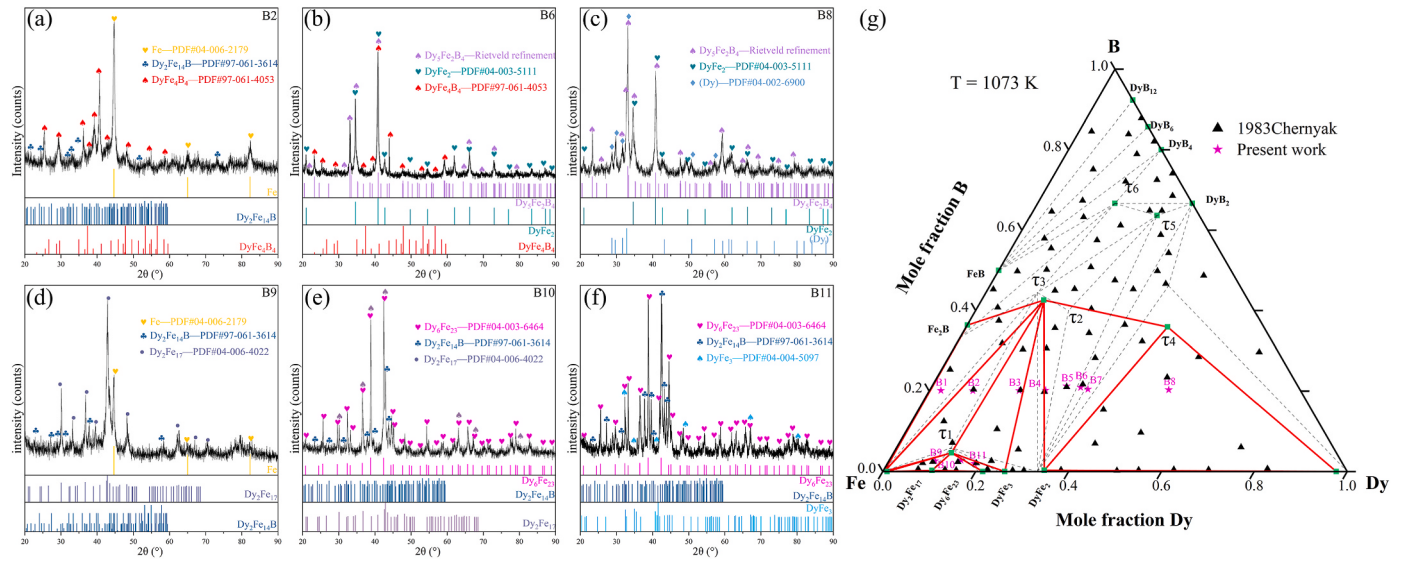


**Fig. 6.** The XRD results of the representative alloys (a–f): A1, A2, A3, A4, A7 and A11; (g) The experimentally determined isothermal sections of the Dy-Fe-B system at 1073 K.

**Table 5**

Phase names and thermodynamic parameters of the Dy-Fe-B system. Gibbs energy is given in J per mole of formula units (given by the sublattice definition), temperature (T) in Kelvin.

Phase	Thermodynamic parameters	
Liquid	$I_{\text{B},\text{Dy},\text{Fe}}^{\text{Liq}}$	$L_{\text{B},\text{Dy},\text{Fe}}^{\text{Liq}} = -67977.6$ , $L_{\text{B},\text{Dy},\text{Fe}}^{\text{Liq}} = 147180.8$ , $L_{\text{B},\text{Dy},\text{Fe}}^{\text{Liq}} = -186500$
Bcc_A2	$G_{\text{Dy},\text{B}}^{\text{bcc}}$	$G_{\text{Dy},\text{B}}^{\text{bcc}} = G_{\text{Dy}}^{\text{0,hser}}(\text{T}) + 3G_{\text{B}}^{\text{0,hser}}(\text{T}) + 150000$
Hcp_A3	$G_{\text{Dy},\text{B}}^{\text{hcp}}$	$G_{\text{Dy},\text{B}}^{\text{hcp}} = G_{\text{Dy}}^{\text{0,hser}}(\text{T}) + 0.5G_{\text{B}}^{\text{0,hser}}(\text{T}) + 50000$
τ <sub>1</sub> -Dy <sub>2</sub> Fe <sub>14</sub> B	$G_{\text{Dy},\text{Fe},\text{B}}^{\text{0,Dy2Fe14B}}$	$-12692.3019 - 35.00363T - 0.30968T \ln T + 0.025305T^2 - 5.62E-04T^3 + 0.667005T^{-1} + 1.06289E-06T^4$ ; ( $T < 50$ ) $-20328.4576 - 14.0389T + 5.7563T \ln T - 0.1343T^2 + 1.2805E-04T^3 + 1888.8526T^{-1} - 6.3704E-08T^4$ ( $50 < T < 398$ ) $-17199 + 58.6628T - 12.5284T \ln T - 1.7884E-2T^2 + 3.4991E-6T^3 - 303036.9072T^{-1} - 4.3491E-10T^4$ ( $T > 398$ )
τ <sub>3</sub> -Dy <sub>2</sub> Fe <sub>4</sub> B <sub>4</sub>	$G_{\text{Dy},\text{Fe},\text{B}}^{\text{0,Dy2Fe4B4}}$	$-50674 + 10.6750T + 1/9G_{\text{Dy}}^{\text{0,hser}}(\text{T}) + 4/9G_{\text{Fe}}^{\text{0,hser}}(\text{T}) + 4/9G_{\text{B}}^{\text{0,hser}}(\text{T})$
τ <sub>4</sub> -Dy <sub>5</sub> Fe <sub>2</sub> B <sub>4</sub>	$G_{\text{Dy},\text{Fe},\text{B}}^{\text{0,Dy5Fe2B4}}$	$-40000 + 8.6588T + 5/11G_{\text{Dy}}^{\text{0,hser}}(\text{T}) + 2/11G_{\text{Fe}}^{\text{0,hser}}(\text{T}) + 4/11G_{\text{B}}^{\text{0,hser}}(\text{T})$
τ <sub>5</sub> -Dy <sub>3</sub> FeB <sub>7</sub>	$G_{\text{Dy},\text{Fe},\text{B}}^{\text{0,Dy3FeB7}}$	$-58159 + 9.8267T + 3/11G_{\text{Dy}}^{\text{0,hser}}(\text{T}) + 1/11G_{\text{Fe}}^{\text{0,hser}}(\text{T}) + 7/11G_{\text{B}}^{\text{0,hser}}(\text{T})$
τ <sub>6</sub> -Dy <sub>2</sub> Fe <sub>4</sub> B	$G_{\text{Dy},\text{Fe},\text{B}}^{\text{0,Dy2Fe4B}}$	$-60776 + 11.4878T + 1/6G_{\text{Dy}}^{\text{0,hser}}(\text{T}) + 1/6G_{\text{Fe}}^{\text{0,hser}}(\text{T}) + 2/3G_{\text{B}}^{\text{0,hser}}(\text{T})$

Dy<sub>2</sub>Fe<sub>17</sub>, DyFe<sub>3</sub>, and τ<sub>1</sub> phases. As presented in Figs. 2(e) and 3(e), DyFe<sub>3</sub>, DyFe<sub>2</sub>, and τ<sub>3</sub> phases exist in alloy A7. Alloy A8 was in the DyFe<sub>3</sub>+DyFe<sub>2</sub>+τ<sub>3</sub> three-phase region too. The τ<sub>2</sub> phase was found, which is against the experimental results by Chernyak et al. [5]. According to their results, alloys A7 and A8 are located in τ<sub>1</sub>+τ<sub>3</sub>+DyFe<sub>2</sub>, τ<sub>2</sub>+τ<sub>3</sub>+DyFe<sub>2</sub> three-phase regions, respectively. Fig. 2(f) shows that alloy A11 is composed of Liquid, DyFe<sub>2</sub> and τ<sub>4</sub> phases, which is inconsistent with the XRD patterns as shown Fig. 3(f). The EPMA analysis of the circular white phase in alloy A11 showed a Dy content of 85 wt% which is lower than the Dy content (97 wt%) in alloy B8 confirming it as the liquid phase. The composition of τ<sub>4</sub> phase is 43.97 at.% Dy, 19.03 at.% Fe and 37.01 at.% B, which slightly deviates from Dy<sub>2</sub>Fe<sub>3</sub> by Chernyak et al. [5]. However, the τ<sub>4</sub> phase compositions measured in the alloys B4-B8 are consistent with the values obtained for alloy A11 as shown in Table 3. The stoichiometry of the τ<sub>4</sub> phase was determined to be Dy<sub>44</sub>Fe<sub>20</sub>B<sub>36</sub>. In the present work, the τ<sub>4</sub> phase was modeled as Dy<sub>5</sub>Fe<sub>2</sub>B<sub>4</sub>. For further verification, Rietveld refinement was performed on powder XRD data retrieved from B8 alloy by Fullprof software. The DyFe<sub>2</sub> and (αDy) phases were treated in a profile matching mode, refining only the unit cell parameters. The Rietveld refinement of X-structure yielded agreement factors of  $R_p = 9.47\%$ ,  $R_{wp} = 11.99\%$ . The details of the Rietveld refinement are summarized in Table 4. Calculated XRD patterns based on the proposed model and observed X-ray diffraction profiles are shown in Fig. 4.

On the Fe-Dy rich side of the Fe-Dy-B system, the present results

differ from those of Chernyak et al. [5]. The most notable difference is the absence of τ<sub>2</sub> phase. Chernyak et al. annealed their alloys at 1073 K for 29 days [5], while the present study extended the annealing duration to 60 days at both 1073 K and 1173 K. Furthermore, the τ<sub>2</sub> phase was only solely identified by XRD from Chernyak et al. [5]. In this work, the Fe-rich side of the Dy-Fe-B system was investigated using XRD and SEM-EPMA. Additionally, the DFT calculations from open databases such as The Open Quantum Materials Database (OQMD) [19–21], indicate that τ<sub>2</sub> phase is not a stable compound which supports the present results. Therefore, the experimental findings presented in this work are considered more reliable.

Using the data in Table 2, the isothermal section of the Dy-Fe-B system at 1173 K on the Fe-rich side was constructed as shown in Fig. 3(g). Three ternary compounds, τ<sub>1</sub>, τ<sub>3</sub>, and τ<sub>4</sub> were identified while the τ<sub>2</sub> phase was not observed.

### 3.1.3. Phase equilibria at 1073 K

Alloys B1-B11 were prepared to determine the isothermal section of the Dy-Fe-B system at 1073 K. The phase compositions and microstructures were measured by SEM-EPMA and XRD. The experimental results are summarized in Table 3. Fig. 5(a–f) and 6(a–f) present the BSE images and XRD patterns of representative alloys B2, B6, B8, B9, B10, and B11, which were annealed at 1073 K for 60 days.

As shown in Figs. 5(a)–6(a), three phases were observed in alloy B2. EPMA measurements identified two prominent phases as (αFe) and τ<sub>3</sub>

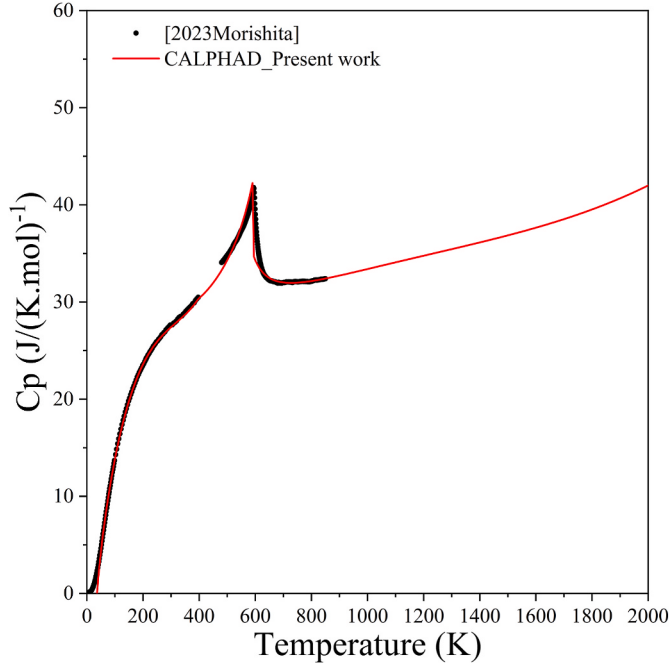


**Fig. 7.** The calculated heat capacity for the  $\text{Dy}_2\text{Fe}_{14}\text{B}$  compared with experimental data from Morishita et al. [18].

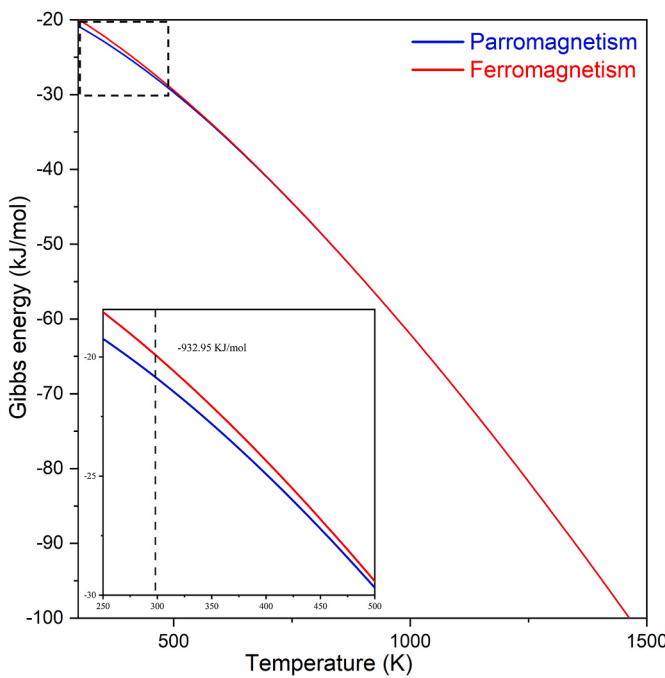


**Fig. 8.** The Gibbs energies of the  $\text{Dy}_2\text{Fe}_{14}\text{B}$  in the ferromagnetism and paramagnetism state.

phase while the third phase could not be conclusively identified due to its small size and low fraction, combined with weak XRD peak intensity. Compared to the SEM results for alloy A2, the B-rich  $\tau_3$  phase is more prominently observed in alloy B2, attributed to the higher B content(20. at%). The third phase in alloy B2 is identified as  $\tau_1$  phase. Consequently, alloys B2 and A2 are situated in the  $\tau_1+(\alpha\text{Fe})+\tau_3$  three-phase region. This indicates that the growth of the compounds in this system is quite slow. Figs. 5(b)–6(b) illustrate that alloy B6 consists of  $\text{DyFe}_2$ ,  $\tau_3$ , and  $\tau_4$  phases. Similar to alloy B2, the increased B content facilitates the

observation of  $\tau_3$  and  $\tau_4$  phases, with the composition of  $\tau_4$  phase closely matching that measured in alloy A11. The phase relationship in this three-phase region has been well verified. Figs. 5(c)–6(c) illustrate that alloy B8 consists of Liquid,  $\text{DyFe}_2$ , and  $\tau_4$ , which is the same result as alloy A11. Figs. 5(d)–6(d) indicate that alloy B9 consists of ( $\alpha\text{Fe}$ ),  $\text{Dy}_2\text{Fe}_{17}$ , and  $\tau_1$  phases, which is the same as alloy A3. As presented in Figs. 5(e)–6(e),  $\text{Dy}_6\text{Fe}_{23}$ ,  $\text{Dy}_2\text{Fe}_{17}$  phases, and  $\tau_1$  phase exist in alloy B10. It can be seen that the  $\tau_1$  phase is precipitated from the  $\text{Dy}_2\text{Fe}_{17}$  phase. Figs. 5(f)–6(f) show that alloy B11 is composed of  $\text{Dy}_6\text{Fe}_{23}$ ,  $\text{Dy}_2\text{Fe}_{17}$ , and  $\tau_1$  phases, which is the same as alloy A4.

Based on the results summarized in Table 3, the isothermal section of the Dy-Fe-B system at 1073 K of the Fe-rich side was constructed as shown in Fig. 6(g), and compared with the isothermal section reported by Chernyak et al. [5]. The main differences are as follows: (1) The ternary compound  $\text{DyFe}_2\text{B}_2$  reported by Chernyak et al. [5] was not found in the present work; (2) The three three-phase regions of  $\tau_1+\tau_3+\text{DyFe}_3$  and  $\tau_3+\text{DyFe}_3+\text{DyFe}_2$  were measured with greater accuracy; (3) The measured composition for  $\tau_4$  phase deviates slightly from previous reports. The challenges of studying RE-containing systems arise from the slow diffusivity of rare-earth (RE) elements. As shown from the SEM of the representative alloys from the present work, the size of the ternary compounds was small even annealed at 1073 K and 1173 K for 60 days. The alloys by Chernyak et al. [5] annealed at 1073 K for 30 days and analyzed by XRD alone, whereas this study used arc-melted alloys with compositions verified by both SEM-EPMA and XRD, making the present results more reliable.

### 3.2. CALPHAD assessment

The CALPHAD assessment of the Dy-Fe-B system was performed using Thermo-Calc software. The descriptions for the binary subsystems were taken from the literature [12–14], and Table 5 lists phase names, thermodynamic models and parameters from the present work.

Within the rare-earth permanent magnet system, the  $\text{RE}_2\text{Fe}_{14}\text{B}$  phase exhibits robust magnetism and holds substantial research significance. The thermodynamic parameters for the  $\text{Dy}_2\text{Fe}_{14}\text{B}$  compound were evaluated initially using the heat capacity data, Curie temperature, the magnetic moment from Morishita et al. [18] and enthalpy of formation

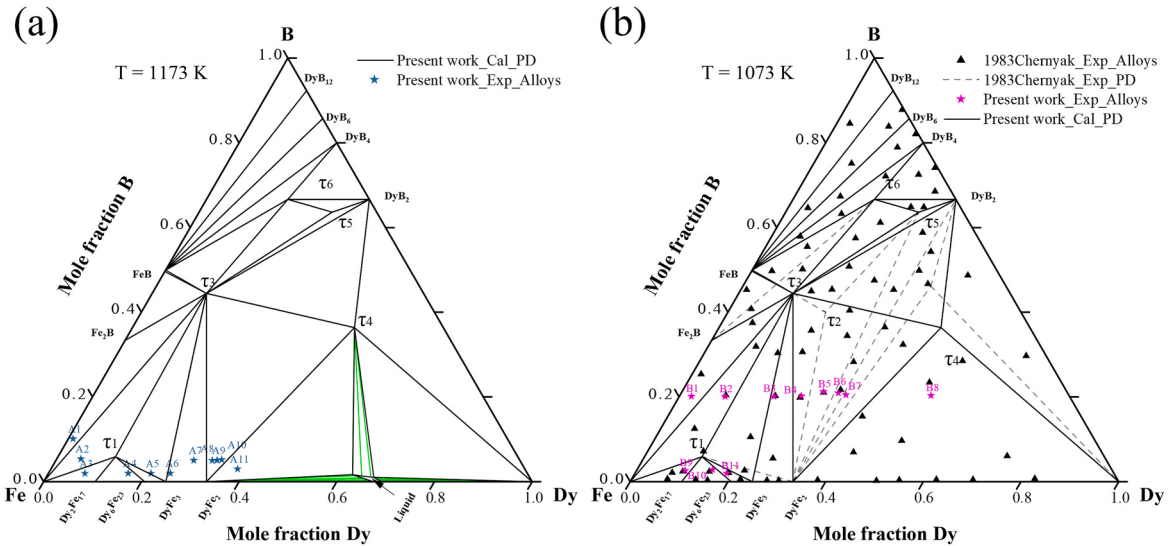


**Fig. 9.** The calculated isothermal sections at (a):1173 K and (b):1073 K.

from the OQMD [19–21]. The calculation process is as follows: First, the contribution of magnetic properties to the Gibbs energy at the corresponding temperature is subtracted using the heat capacity data from Morishita et al. [18]. Subsequently, the data are fitted and computed to derive the Gibbs energy expression of  $\text{Dy}_2\text{Fe}_{14}\text{B}$  in the nonmagnetic state.

The Curie temperature and magnetic moment were defined as 594.1 K and 0.59  $\mu\text{B}/\text{atom}$ , respectively. The calculated heat capacity, shown in Fig. 7, was compared with experimental data from Morishita et al. [18]. The Gibbs energies of the  $\text{Dy}_2\text{Fe}_{14}\text{B}$  in the ferromagnetic and paramagnetic state are shown in Fig. 8. The calculation results show a difference of approximately 0.941 kJ/mol between the Gibbs energies of ferromagnetic and paramagnetic at the Curie temperature.

For the thermodynamic description of other ternary compounds, parameter A was derived from calculated results from various open databases [22–24], while parameter B utilizes the thermodynamically optimized results. As the experimental section of this work did not yield samples rich in the B end, the structures of ternary compounds  $\tau_5$  and  $\tau_6$  from previous work were directly employed, with computational results from open databases through the OQMD being utilized. In this work, the stoichiometric ratio of  $\tau_4$  phases was adjusted to  $\text{Dy}_5\text{Fe}_2\text{B}_4$  accordingly.

Fig. 9 presents the comparison of the calculated isothermal sections at 1173 K and 1073 K with the experimental results obtained in this work and reported by Chernyak et al. [5]. As shown in Fig. 9(a), the calculated phase equilibria at 1173 K align closely with the experimental results obtained in this work. The liquid phase was observed at 1173 K. The calculated isothermal sections are consistent with the present work while showing some differences from Chernyak et al. for the Fe-rich side [5]. The three-phase equilibria in the rich-B side closely resemble the experimental results reported by Chernyak et al. [5]. As previously noted, the experimental results reported by Chernyak et al. [5] contain inaccuracies. Some deviations were identified on the B-rich side. Further study for the B-rich is necessary.

Fig. 10 compares the calculated isopleths compared with experimental data from Grieb et al. [6]. Two sections at constant Fe content 78 and 82.35 at.% (Fig. 10(a)–(b)), and two sections at  $\text{Dy:B} = 2:1$  (Fig. 10(c)) and  $\text{Fe:Dy} = 17:2$  (Fig. 10(d)) were constructed by Grieb et al. [6]. As shown in Fig. 10(a), the calculated liquidus agrees well with the

experimental results. For  $x(\text{Fe}) = 0.8235$  as shown in Fig. 10(b), the calculated liquidus and solid-phase reaction temperatures were well matched with the experimental results. The liquidus and solid-phase reaction for  $\text{Fe:Dy} = 17:2$  as shown in Fig. 10(c) are in good agreement with the experimental results. The liquidus and solid phase reaction temperatures at 1380 K (at  $\text{Dy:B} = 2:1$  (Fig. 10(d))) are in good agreement with the experimental results. In general, the present calculation in this work describes the experimental data well.

Fig. 11 shows the calculated liquidus surface projection of the Dy-Fe-B ternary system. Five saddle points were identified in the liquidus projection:  $m_1$  (8.70 at.% Dy, 35.31 at.% B) at 1635.8 K,  $m_2$  (58.58 at.% Dy, 3.48 at.% B) at 956.2 K,  $m_3$  (12.68 at.% Dy, 9.84 at.% B) at 1226.4 K,  $m_4$  (8.02 at.% Dy, 31.83 at.% B) at 1504.7 K and  $m_5$  (11.55 at.% Dy, 16.32 at.% B) at 1160.4 K, respectively. The calculated compositions and temperatures of the invariant reactions are summarized in Table 6. Further experiments still need to be performed to confirm the current findings.

#### 4. Conclusions

The isothermal sections at 1173 K and 1073 K of the Dy-Fe-B system were constructed using EPMA and XRD techniques, revealing seven three-phase regions. The metastable  $\text{Fe}_3\text{B}$  phase form for alloys containing 12 to 25 at.% B during quenching. On the Dy-Fe rich side, three ternary compounds  $\tau_1$ ,  $\tau_3$ , and  $\tau_4$  were determined with three three-phase regions of  $\tau_1+\tau_3+\text{DyFe}_3$ ,  $\tau_3+\text{DyFe}_3+\text{DyFe}_2$ , and  $\tau_3+\tau_4+\text{DyFe}_2$  measured more accurately than the previous studies. The ternary compound  $\tau_2$  was not observed at 1073 K and 1173 K. Utilizing experimental information from this work and existing literature, thermodynamic modeling of the Dy-Fe-B system was performed. A self-consistent set of thermodynamic parameters was derived, accurately reproducing most experimental data.

#### CRediT authorship contribution statement

**Wei Yang:** Writing – original draft, Investigation. **Yiwei Wang:** Investigation. **Shuhong Liu:** Project administration. **Peisheng Wang:** Writing – review & editing, Supervision, Software, Methodology. **Wei**

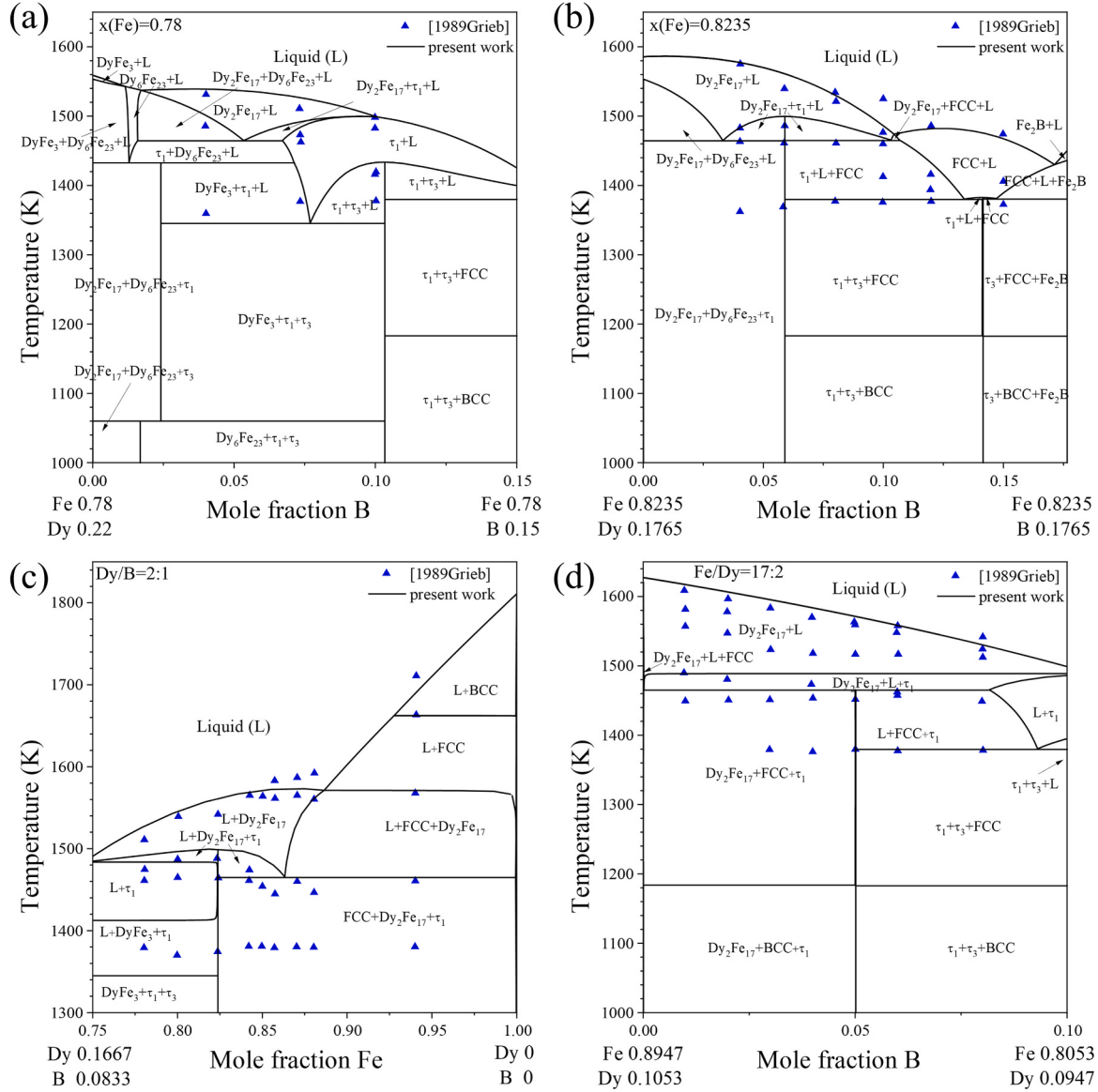


**Fig. 10.** Calculated vertical section in the Dy–Fe–B system compared with experimental data: (a) 78 at.% Fe; (b) 82.35 at.% Fe; (c) Dy:B = 2:1; (d) Fe:Dy = 17:2.

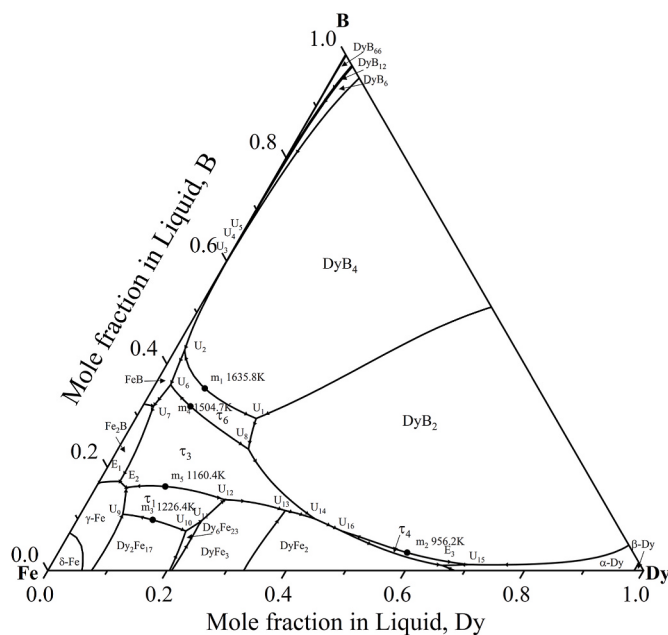


**Fig. 11.** The calculated liquidus surface projection of the Dy-Fe-B ternary system.

**Table 6**  
Invariant reactions of the Dy-Fe-B ternary system calculated in this work.

Invariant reactions	Type	T(K)	Composition	
			x(Dy)	x(Fe)
L + DyB <sub>4</sub> ↔ τ <sub>6</sub> + DyB <sub>2</sub>	U <sub>1</sub>	1840.43	0.2023	0.5030
L + DyB <sub>4</sub> ↔ τ <sub>6</sub> + FeB	U <sub>2</sub>	1830.74	0.0161	0.5560
L + DyB <sub>4</sub> ↔ FeB + DyB <sub>6</sub>	U <sub>3</sub>	1827.67	0.0006	0.4037
L + DyB <sub>6</sub> ↔ FeB + DyB <sub>12</sub>	U <sub>4</sub>	1797.48	0.0002	0.3779
L + DyB <sub>12</sub> ↔ FeB + DyB <sub>66</sub>	U <sub>5</sub>	1781.11	0.0001	0.3659
L + τ <sub>6</sub> ↔ τ <sub>3</sub> + FeB	U <sub>6</sub>	1720.53	0.0262	0.6136
L + FeB ↔ τ <sub>3</sub> + Fe <sub>2</sub> B	U <sub>7</sub>	1630.98	0.0180	0.6632
L + τ <sub>6</sub> ↔ τ <sub>3</sub> + Dy <sub>2</sub> B	U <sub>8</sub>	1615.84	0.2191	0.5455
L + Dy <sub>2</sub> Fe <sub>17</sub> ↔ τ <sub>1</sub> + γFe	U <sub>9</sub>	1465.45	0.0713	0.8194
L + Dy <sub>2</sub> Fe <sub>17</sub> ↔ τ <sub>1</sub> + Dy <sub>6</sub> Fe <sub>23</sub>	U <sub>10</sub>	1464.83	0.1933	0.7300
L + Dy <sub>6</sub> Fe <sub>23</sub> ↔ τ <sub>1</sub> + DyFe <sub>3</sub>	U <sub>11</sub>	1433.16	0.2089	0.6960
L ↔ τ <sub>3</sub> + γFe + Fe <sub>2</sub> B	E <sub>1</sub>	1380.98	0.0346	0.7926
L ↔ τ <sub>3</sub> + τ <sub>1</sub> + γFe	E <sub>2</sub>	1380.26	0.0515	0.7877
L + τ <sub>1</sub> ↔ DyFe <sub>3</sub> + τ <sub>3</sub>	U <sub>12</sub>	1345.90	0.2278	0.6348
L + DyFe <sub>3</sub> ↔ DyFe <sub>2</sub> + τ <sub>3</sub>	U <sub>13</sub>	1271.21	0.3404	0.5432
L + τ <sub>3</sub> ↔ DyFe <sub>2</sub> + Dy <sub>2</sub> B	U <sub>14</sub>	1237.08	0.3981	0.5015
L + Dy <sub>2</sub> B ↔ αDy + τ <sub>4</sub>	U <sub>15</sub>	1220.17	0.7010	0.2875
L + Dy <sub>2</sub> B ↔ τ <sub>4</sub> + DyFe <sub>2</sub>	U <sub>16</sub>	1218.14	0.4543	0.4686
L ↔ αDy + τ <sub>4</sub> + DyFe <sub>2</sub>	E <sub>3</sub>	1151.19	0.6573	0.3328

**Zhai:** Project administration.

#### Declaration of competing interest

The authors declare that they have no known competing financial interests or personal relationships that could have appeared to influence the work reported in this paper.

#### Acknowledgment

The financial support from the National key research and development program of China (2021YFB3502600) and Major Special Projects in Changsha Science and Technology Bureau (Grant No kh2103011) are greatly acknowledged.

#### Appendix A. Supplementary data

Supplementary data to this article can be found online at <https://doi.org/10.1016/j.calphad.2025.102826>.

#### Data availability

Data will be made available on request.

#### References

- [1] J.J. Croat, J.F. Herbst, R.W. Lee, F.E. Pinkerton, Pr-Fe and Nd-Fe-based materials: a new class of high-performance permanent magnets, *J. Appl. Phys.* 55 (1984) 2078–2082.
- [2] M. Sagawa, S. Fujimura, N. Togawa, H. Yamamoto, Y. Matsuura, New material for permanent magnets on a base of Nd and Fe, *J. Appl. Phys.* 55 (1984) 2083–2087.
- [3] L. Liu, H. Sepehri-Amin, T. Ohkubo, M. Yano, A. Kato, N. Sakuma, T. Shoji, K. Hono, Coercivity enhancement of hot-deformed Nd-Fe-B magnets by the eutectic grain boundary diffusion process using Nd62Dy20Al18 alloy, *Scr. Mater.* 129 (2017) 44–47.
- [4] J.F. Herbst, R2Fe14B materials: intrinsic properties and technological aspects, *Rev. Mod. Phys.* 63 (1991) 819–898.
- [5] G. Cherryak, N. Chaban, Y.B. Kuz'ma, *Ternary [Dy, Er]-Fe-B Systems*, Poroshkovaya Metallurgiya (Kiev), 1983, pp. 65–66.
- [6] B. Grieb, G. Mueller, E. Henig, G. Petzow, H. Stadelmaier, Fe sub 17 Dy sub 2 and Fe sub 17 Tb sub 2 with dissolved boron, *Z. Metallkd.* (1989) 80.
- [7] M.-A. Van Ende, I.-H. Jung, Y.-H. Kim, T.-S. Kim, Thermodynamic optimization of the Dy-Nd-Fe-B system and application in the recovery and recycling of rare earth metals from NdFeB magnet, *Green Chem.* 17 (2015) 2246–2262.
- [8] T. Abe, M. Morishita, Y. Chen, A. Saengdeejing, K. Hashimoto, Y. Kobayashi, I. Ohnuma, T. Koyama, S. Hirosawa, Development of a prototype thermodynamic database for Nd-Fe-B permanent magnets, *Sci. Technol. Adv. Mater.* 22 (2021) 557–570.
- [9] Z. Dai, K. Li, Z. Wang, W. Liu, Z. Zhang, Magnetic-property assessment on Dy-Nd-Fe-B permanent magnet by thermodynamic calculation and micromagnetic simulation, *Materials* 15 (2022) 7648.
- [10] Scientific Group Thermodata Europe: SGTE, <https://www.sgte.net/en/free-pure-substance-database>, visited 20-March-2025.
- [11] O. Redlich, A. Kister, Algebraic representation of thermodynamic properties and the classification of solutions, *Ind. Eng. Chem.* 40 (1948) 345–348.
- [12] M.H. Rong, X.L. Chen, J. Wang, G.H. Rao, H.Y. Zhou, Thermodynamic re-assessment of the Fe-Dy and Fe-Tb binary systems, *Calphad* 59 (2017) 154–163.
- [13] S. Li, M.H. Rong, L. Xu, Q. Wei, J. Wang, G.H. Rao, H.Y. Zhou, Thermodynamic assessment of the RE-B (RE = Ce, Dy, Lu) binary systems, *Calphad* 68 (2020) 101740.
- [14] V.T. Witiusiewicz, A.A. Bondar, U. Hecht, A. Theofilatos, N.I. Tsyganenko, S. V. Utkin, I.B. Tikhonova, Experimental study and thermodynamic re-modelling of the constituent binaries and ternary B-Fe-Ti system, *J. Alloys Compd.* 800 (2019) 419–449.
- [15] G. Inden, Magnetically induced heterogeneities with tricritical point in FCC CoV alloys, *Scripta Metall.* 15 (1981) 669–671.
- [16] M. Hillert, M. Jarl, A model for alloying in ferromagnetic metals, *Calphad* 2 (1978) 227–238.
- [17] M. Palumbo, G. Cacciamani, E. Bosco, M. Baricco, Thermodynamic analysis of glass formation in Fe-B system, *Calphad* 25 (2001) 625–637.
- [18] M. Morishita, T. Abe, H. Yamamoto, A. Nozaki, S. Kimura, Thermodynamic and magnetic properties for Dy2Fe14B determined by heat capacity measurement from very low to high temperatures and solution calorimetry, *Thermochim. Acta* 721 (2023) 179410.
- [19] J.E. Saal, S. Kirklin, M. Aykol, B. Meredig, C. Wolverton, Materials design and discovery with high-throughput density functional theory: the open Quantum materials database (OQMD), *JOM* 65 (2013) 1501–1509.
- [20] S. Kirklin, J.E. Saal, B. Meredig, A. Thompson, J.W. Doak, M. Aykol, S. Rühl, C. Wolverton, The Open Quantum Materials Database (OQMD): assessing the accuracy of DFT formation energies, *npj Comput. Mater.* 1 (2015) 15010.
- [21] OQMD: The Open Quantum Materials Database, <http://oqmd.org/>, visited 20-March-2025.
- [22] C.W. Andersen, R. Armiento, E. Blokhin, G.J. Conduit, S. Dwaraknath, M.L. Evans, Á. Fekete, A. Gopakumar, S. Gražulis, A. Merkys, F. Mohamed, C. Oses, G. Pizzi, G. M. Rignanese, M. Scheidgen, L. Talirz, C. Toher, D. Winston, R. Aversa, K. Choudhary, P. Colinet, S. Curtarolo, D. Di Stefano, C. Draxl, S. Er, M. Esters, M. Fornari, M. Giantomassi, M. Govoni, G. Hautier, V. Hegde, M.K. Horton, P. Huck, G. Huhs, J. Hummelshøj, A. Kariryaa, B. Kozinsky, S. Kumbhar, M. Liu, N. Marzari, A.J. Morris, A.A. Mostofi, K.A. Persson, G. Petretto, T. Purcell, F. Ricci, F. Rose, M. Scheffler, D. Speckhard, M. Uhrin, A. Vaitkus, P. Villars, D. Waroquiers, C. Wolverton, M. Wu, X. Yang, OPTIMADE, an API for exchanging materials data, *Sci. Data* 8 (2021) 217.
- [23] S.-D. Xue, Q.-J. Hong, Materials properties prediction (MAPP): empowering the prediction of material properties solely based on chemical formulas, *Materials* 17 (2024) 4176.
- [24] ML data for crystals:<http://mat-x.org>.

- [25] V.V. Novikov, T.A. Chukina, A.A. Verevkin, Anomalies in thermal expansion of rare-earth diborides in the temperature range of magnetic phase transformations, *Phys. Solid State* 52 (2010) 364–369.
- [26] R.W. Cahn, in: T.B. Massalski, H. Okamoto, P.R. Subramanian, L. Kacprzak (Eds.), *Binary Alloy Phase Diagrams*, second ed. vol. 3, ASM International, Materials Park, Ohio, USA, 1991, pp. 628–629. December 1990. xxii, 3589 pp., 3 vol., hard- back. \$995.00 the set, Advanced Materials.
- [27] H. Werheit, U. Kuhlmann, M. Laux, T. Lundström, Structural and electronic properties of carbon-doped  $\beta$ -rhombohedral boron, *Phys. Status Solidi* 179 (1993) 489–511.
- [28] A.S. van der Goot, K.H.J. Buschow, The dysprosium-iron system: structural and magnetic properties of dysprosium-iron compounds, *J. Less Common Metals* 21 (1970) 151–157.
- [29] J. Etourneau, J.P. Mercurio, A. Berrada, P. Hagenmuller, R. Georges, R. Bourezg, J. C. Gianduzzo, The magnetic and electrical properties of some rare earth tetraborides, *J. Less Common Metals* 67 (1979) 531–539.
- [30] A. Malfliet, G. Cacciamani, N. Lebrun, P. Rogl, Boron – iron – neodymium. Landolt-Börnstein - Group IV Physical Chemistry, Springer, Berlin Heidelberg, 2008, pp. 482–511.
- [31] J. Herbst, W. Yelon, Crystal and magnetic structure of Pr<sub>2</sub>Fe<sub>14</sub>B and Dy<sub>2</sub>Fe<sub>14</sub>B, *J. Appl. Phys.* 57 (1985) 2343–2345.
- [32] G. Stepanchikova, Y.B. Kuz'ma, B. Chernyak, New borides with structure of CeAl<sub>2</sub>Ga<sub>2</sub> type, dopov. Akad. Nauk Ukr. RSR, Ser. A: Fiz.-Mat. Tekh. Nauki (1978) 950–953.
- [33] D. Givord, P. Tenaud, J. Moreau, Refinement of the crystal structure of R<sub>1</sub>+eFe<sub>4</sub>B<sub>4</sub> compounds (R≡ Nd, Gd), *Journal of the Less Common Metals* 123 (1986) 109–116.
- [34] D. De Mooij, K. Buschow, Note on the structure and composition of the B-rich ternary phase in the Nd-Fe-B system, *Philips J. Res.* 43 (1988) 70–74.
- [35] O. Dub, N. Chaban, Y.B. Kuz'ma, New borides of Pr<sub>5</sub>–XCo<sub>2</sub>–XB<sub>6</sub>-type structure containing iron and cobalt, *J. Less Common Metals* 117 (1986) 297–302.
- [36] G. Chernyak, N. Chaban, Y.B. Kuz'ma, Ternary systems {Dy, Er}-Fe-B, soviet powder metallurgy and metal, *Ceramics* 22 (1983) 479–480.